iJETRM
INTERNATIONAL JOURNAL OF ENGINEERING TECHNOLOGY RESEARCH & MANAGEMENT (IJETRM)
https://ijetrm.com/

CONTINUOUS-POWER RF BOUNDARY INTERVENTION FOR ATTRIBUTING ELECTRICAL ANOMALIES TO FIXED WIRING OR LOAD-SIDE EQUIPMENT: THEORY, CALIBRATED CHARACTERISATION, AND BLINDED EVALUATION

Vamshi Teja Sara
Avalon Artificial Intelligence Limited, Middlesbrough, United Kingdom
vamsi@unitedavalon.com

Author Biography / Patent Declaration:

V. T. Sara is affiliated with Avalon Artificial Intelligence Limited, Middlesbrough, United Kingdom (e-mail: vamsi@unitedavalon.com). The method described in this paper is the subject of UK Patent Application No. GB 2625992.9, filed on 2 November 2026.

ABSTRACT

Protective devices disconnect the supply when a hazard is detected but do not indicate whether an anomaly originates in the fixed premises wiring, the connected equipment or the interface between them. This paper formulates source attribution as selective classification with a reject option and studies a continuous-power radio-frequency (RF) boundary: a device that keeps an unswitched power path in circuit while a separate RF path is switched between through and shadow states. A two-port analysis shows that the isolation of such a boundary is limited by the power path and terminations rather than by the switch, and yields a criterion for selecting the diagnostic band. In an unpowered bench characterisation, a boundary with a 47 µH power path permanently connected changed the house-to-load transmission by −22.5 dB over 190–300 MHz, repeatably to 0.021 dB and within 0.55 dB of a model built from separately measured components. Two blinded trials on a 25 m line analogue with resistive series substitutes followed. In the first, every wiring-side substitute was attributed to the fixed wiring, and thresholds were shown to require baselines that capture handling variability; the second trial showed that load-side attribution requires a redesigned load-side observation point. Across both trials, the wiring-side substitute was completely separated from the other conditions on the house-end residual (8 versus 15 trials; AUC = 1.0; post hoc) and appeared as a time-domain peak close to the house-end reference plane. The results establish the bench basis of the method and define its extension to two-sided attribution.

Keywords

Electrical fault diagnosis, fault attribution, reflectometry, time-domain reflectometry, S-parameters, vector network analysis, RF switching, selective classification, reject option, blinded evaluation, measurement uncertainty.

I. INTRODUCTION

Series faults in low-voltage installations, including loose terminals, degraded crimps, corroded contacts and damaged flexible cords, can develop gradually. A high-resistance joint dissipates power locally, oxidises, and may eventually arc. Protective devices are designed to respond to the consequences: circuit breakers to over-current, residual-current devices to earth leakage, and arc-fault detection devices (AFDDs) to the electrical signatures of arcing [1]. Their purpose is protection, and their action is disconnection.

Once protection has acted, the person responsible must decide what to repair, and responsibility often follows physical location. In the UK, for example, the fixed installation, governed by wiring regulations such as BS 7671 [2], is the responsibility of the owner and requires a qualified electrician; an appliance and its cord are the responsibility of their owner; sockets, plugs and adapters sit at the interface. Misattribution sends the wrong trade, replaces the wrong component, or leaves a hazardous fault in service. Determining the source conventionally requires isolating and testing the circuit, and this creates a methodological problem: intermittent faults may depend on load current, temperature or mechanical stress, and may be absent once the circuit is de-energised. The diagnostic act can destroy the evidence it seeks.

Radio-frequency (RF) reflectometry is attractive because it is non-disruptive. A conductor pair is a transmission line at RF, and impedance discontinuities reflect injected energy [3]; reflectometric methods are well established for locating wiring faults [4], [5]. A reflectometer at one point of an installation, however, observes the superposition of the wiring, every connection, and the load. Its response indicates that something has changed,

 © Author(s) | CC BY 4.0 International License.

iJETRM
INTERNATIONAL JOURNAL OF ENGINEERING TECHNOLOGY RESEARCH & MANAGEMENT (IJETRM)
https://ijetrm.com/

not on which side of a given connection point the change lies. Separating the sides would ordinarily require disconnecting one of them.

This paper addresses that limitation by introducing a *controllable RF boundary* between the premises wiring and the load while the power path remains continuously in circuit. The work is guided by three research questions:

- **RQ1:** Can an RF diagnostic path be switched across a boundary whose power path is never interrupted, producing a large, repeatable and predictable change in house-to-load RF isolation that can be measured in place?
- **RQ2:** Does a series anomaly on the house side of such a boundary produce a signature that is separable from the no-fault and load-side conditions, persists when the load side is RF-isolated, and where does it appear relative to the boundary?
- **RQ3:** What are the requirements for attributing load-side anomalies, and does the decision logic behave safely when they are not met?

The contributions are as follows.

1) A formulation of electrical-anomaly source attribution as selective classification over house-side, load-side and interface hypotheses with a mandatory reject option, and a corresponding system architecture and method (Sections III and V).
2) A two-port theory of the continuous-power boundary, including an isolation limit showing that the power path, not the switch, limits isolation, and a criterion for selecting the diagnostic band (Section IV).
3) A calibrated, unpowered bench characterisation of the switching network, candidate power-path inductors and an assembled boundary, with an uncertainty analysis and a comparison between measurement and a component-level model (Sections VI and VII).
4) Two blinded trials on a 25 m line analogue, which identify the threshold and load-side design requirements, and a post hoc analysis showing that a wiring-side series substitute is separable on the house-end residual and appears close to the house-end reference plane in the time domain (Section VII).
5) An analysis of the requirements for load-side attribution, derived from the load-side observations (Sections VII and VIII).

The remainder of the paper is organised as follows. Section II reviews related work. Section III formulates the problem. Section IV develops the boundary theory. Section V describes the diagnostic method. Section VI details the experimental methodology. Section VII presents the results. Section VIII discusses them, Section IX states the limitations, and Section XI concludes.

II. Background and Related Work

A. Protective Devices and Arc-Fault Detection

Arc-fault detection devices are standardised in BS EN 62606 [1] and detect characteristic current or high-frequency signatures of series and parallel arcing. Sapir [7] monitors RF transients on the supply line, converts transients above a threshold into pulses, analyses their timing and duration to distinguish arcing from switching events, and accumulates evidence to raise an alarm or trip a breaker. Eriksen et al. [8] describe receptacles that monitor variance in input power and disconnect the output when it leaves a threshold range. These approaches protect effectively but are designed to detect and, where necessary, disconnect; they do not determine whether the cause lies in the fixed wiring or in the equipment, and their protective action interrupts the supply.

B. Reflectometry for Wiring Faults

Time-domain reflectometry (TDR), frequency-domain reflectometry (FDR), and spread-spectrum and noise-domain variants have been compared for locating faults in wiring [4]. Spread-spectrum TDR enables measurement on live wires by embedding a low-level code below the noise of the operating signal [5]. These techniques locate discontinuities along a wire from a single access point but do not provide a controllable separation between the installation and the connected equipment.

C. Power-Line Channels

Power-line communication research has produced multipath models of the low-voltage network at high frequencies, in which branches and impedance mismatches create echoes and frequency-selective fading [6]. These models explain why responses at one point of an installation combine contributions from many elements, which motivates the boundary studied here.

D. Monitoring Systems in the Patent Literature

Related patents describe interconnect status monitoring [9], RF process-sensing networks [10], multi-information fusion for circuit-breaker diagnosis [11] and ingress-noise localisation in cable networks [12]. To the author's knowledge, none combines an unswitched power path with a switchable RF boundary, measured bidirectional isolation, state-invariance verification and three-hypothesis attribution with abstention.

 © Author(s) | CC BY 4.0 International License.

iJETRM
INTERNATIONAL JOURNAL OF ENGINEERING TECHNOLOGY RESEARCH & MANAGEMENT (IJETRM)
https://ijetrm.com/

E. Classification with a Reject Option

Chow [13] characterised the optimum trade-off between error and rejection for a classifier allowed to withhold decisions. Selective classification makes the coverage–risk trade-off explicit and seeks to guarantee a target risk on the accepted subset [14]. For fault attribution, a confident but wrong decision can be more harmful than none, which makes a principled reject option a natural design requirement.

Table I summarises the capabilities targeted by this work relative to the categories above.

TABLE I: Positioning Relative to Existing Approaches

Capability	AFDD [1], [7]	Reflectometry [4], [5]	Monitoring [8], [9]	This work
Locates source without disconnecting	No	Partly[a]	No[b]	By design[c]
Controllable house/load separation	No	No	No	Yes (bench)
Separation measured in place	–	–	–	Yes (bench)
Interface as a distinct hypothesis	No	No	No	Formulated[c]
Mandatory reject option	No	No	No	Yes

[a]Locates discontinuities along a wire; live-wire variants exist [5]. [b]Disconnects on threshold [8]. [c]Not yet demonstrated: the bench study was unpowered and did not evaluate the interface hypothesis.

III. PROBLEM FORMULATION

A. Installation and Hypotheses

Consider a circuit in which a supply feeds fixed premises wiring that terminates at a connection point, beyond which load-side equipment is connected. Let an anomaly be a change in a series impedance somewhere in the circuit. We define four hypotheses:

- H_0: no anomaly;
- H_W: the anomaly is in the fixed wiring (house side);
- H_L: the anomaly is in the load-side equipment;
- H_I: the anomaly is at the interface (the boundary device or the connection between it and the load).

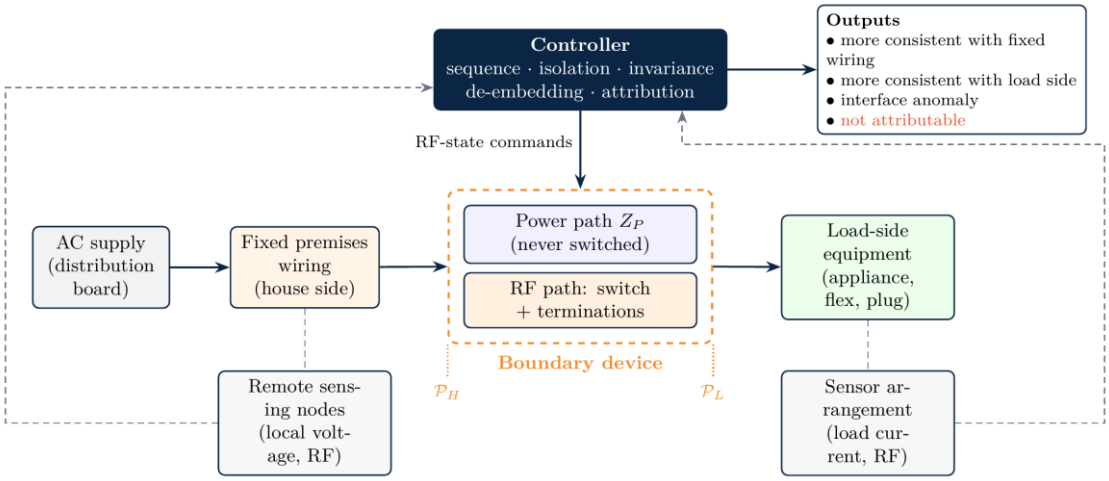


Fig. 1. System architecture. The boundary device separates the house side from the load side with an unswitched power path and a separately switchable RF path, defining the reference planes $\mathcal{P}_H$ and $\mathcal{P}_L$. Sensing (dashed) feeds the controller, which sequences the RF path, measures the isolation achieved, verifies state invariance, and outputs an attribution or abstains. Conceptual: the bench study of Sections VI–VII implements the boundary and the measurements, with the RF state set by hand and no controller or sensing nodes.

B. Observables

As shown in Fig. 1, a boundary device at the connection point defines a house-side reference plane $\mathcal{P}_H$ and a load-side reference plane $\mathcal{P}_L$. In each RF state $s \in \{0, S\}$ (RF-through and RF-shadow) and at frequencies f_k, $k = 1, \ldots, K$, the system observes reflection coefficients $S_{11}^{(v,s)}(f_k)$ at view $v \in \{H, L\}$, transmission coefficients across

 © Author(s) | CC BY 4.0 International License.

iJETRM
INTERNATIONAL JOURNAL OF ENGINEERING TECHNOLOGY RESEARCH & MANAGEMENT (IJETRM)
https://ijetrm.com/

the boundary in both directions, and a vector of protected state variables $\mathbf{q}$ (load current, supply voltage, RF noise level and fault-state indicators).

C. Attribution as Selective Classification

An attribution system is a pair (g, ρ) of a classifier $g: \mathcal{X} \to \{H_0, H_W, H_L, H_I\}$ and a selection function $\rho: \mathcal{X} \to \{0,1\}$, where $\rho = 0$ produces the output not attributable. For an observation distribution $\mathcal{D}$, the coverage is $\phi = \mathbb{E}_{\mathcal{D}}[\rho(x)]$ and the selective risk is

$$R(g, \rho) = \frac{\mathbb{E}_{\mathcal{D}}[\ell(g(x), y)\, \rho(x)]}{\phi},$$

where ℓ is the misattribution loss [14]. Because the cost of a false attribution to a side generally exceeds the cost of abstention, the design objective is to keep R below a pre-set bound, accepting reduced coverage. When $\phi = 0$, R is undefined. In this work ρ is defined by physically meaningful validity conditions (Section V) in addition to statistical separation.

D. Design Requirements

The formulation leads to eight requirements, which also define the acceptance criteria of the experimental programme: (R1) do not interrupt the supply; (R2) create a controllable house/load separation; (R3) measure the separation achieved on each occasion; (R4) verify that the state did not change; (R5) remove the hardware's own signature; (R6) treat the interface as a distinct hypothesis; (R7) withhold judgement when the evidence is insufficient; and (R8) complete the diagnosis within the stability window of the fault. Table II summarises the notation.

TABLE II: Notation

Symbol	Meaning
$\mathcal{P}_H$, $\mathcal{P}_L$	House-side and load-side reference planes
O, S	RF-through and RF-shadow states
Z_0	Reference impedance (50 Ω)
Z_P	RF impedance of the power path
Z_H, Z_L	Shadow-state terminations, house and load side
κ	Isolation change, $20\log_{10}(\lvert S_{21}^{S}\rvert/\lvert S_{21}^{O}\rvert)$
$r_{v,s}$	Residual in view v, state s (RMS over band)
$T_{v,s}$	Decision threshold for $r_{v,s}$
ψ	Persistence ratio $r_{H,S}/r_{H,O}$
K, M	Number of frequency points; number of baselines
$\mathcal{B}$	Admissible diagnostic band
τ	Band-selection limit (-10 dB)
$\Delta h(t)$	Time-domain transform of the S_{11} difference
ρ, ϕ	Selection function; coverage
$\boldsymbol{q}$	Protected state variables

IV. Boundary Theory

A. Two-Port Model

Fig. 2 shows the equivalent circuit of the boundary in the RF-shadow state. Between $\mathcal{P}_H$ and $\mathcal{P}_L$ the power path is a series impedance Z_P, which is always present. The switch adds a parallel series path whose impedance is low in RF-through and very high in RF-shadow. In RF-shadow the house port is terminated by Z_H and the load port by Z_L through the switch. Using transmission (ABCD) matrices [3], the shadow-state network is the cascade

$$\begin{bmatrix} A & B \\ C & D \end{bmatrix} = \begin{bmatrix} 1 & 0 \\ Y_H & 1 \end{bmatrix} \begin{bmatrix} 1 & Z_P \\ 0 & 1 \end{bmatrix} \begin{bmatrix} 1 & 0 \\ Y_L & 1 \end{bmatrix}, \qquad (2)$$

with $Y_H = 1/Z_H$ and $Y_L = 1/Z_L$, and the transmission coefficient between Z_0 ports is

$$S_{21} = \frac{2}{A + B/Z_0 + CZ_0 + D}. \qquad (3)$$

 © Author(s) | CC BY 4.0 International License.

iJETRM
INTERNATIONAL JOURNAL OF ENGINEERING TECHNOLOGY RESEARCH & MANAGEMENT (IJETRM)
https://ijetrm.com/

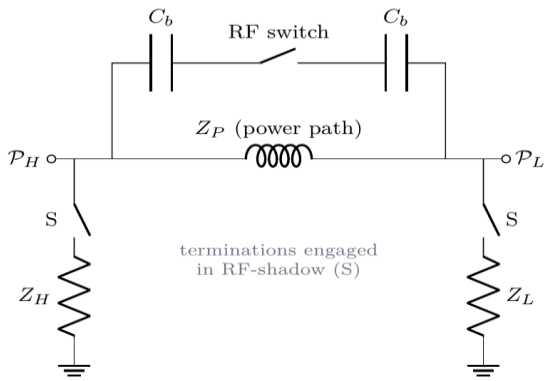


Fig. 2. Equivalent circuit of the boundary between the reference planes. The power path Z_P is permanently connected; the RF switch (with blocking capacitors C_b) is closed in RF-through and open in RF-shadow, where the ports are terminated by Z_H and Z_L.

B. Isolation Limit Set by the Power Path

Proposition 1. *Let the switch be ideal in RF-shadow (open circuit). Then the shadow-state transmission of the boundary equals that of the passive network formed by Z_H, Z_P and Z_L, given by (2)–(3), which is the value approached as the switch's own isolation is increased. In particular:*

1. *without shunt loading of the reference planes ($Y_H = Y_L = 0$),* $|S_{21}^S| = \frac{2Z_0}{|2Z_0+Z_P|}$; (4)
2. *with matched shadow-state terminations ($Z_H = Z_L = Z_0$),* $|S_{21}^S| = \frac{Z_0}{2\,|Z_0+Z_P|}$. (5)

extitProof: An open switch removes its branch, leaving the cascade (2). With $Y_H = Y_L = 0$ one obtains $A = D = 1$, $B = Z_P$, $C = 0$ and hence (4) from (3). With $Y_H = Y_L = 1/Z_0$, writing $p = Z_P/Z_0$, the cascade gives $A = D = 1 + p$, $B = Z_P$ and $C = (2 + p)/Z_0$, so $A + B/Z_0 + CZ_0 + D = 4(1 + p)$ and $S_{21} = 1/(2(1 + p))$, which is (5). A real switch adds a parallel branch of impedance Z_{sw} across Z_P; for $|Z_{sw}| \gg |Z_P|$ its effect is negligible. A reactive branch can, however, resonate with Z_P and change $|S_{21}^S|$ in either direction over a narrow band, so the proposition is stated for the ideal switch. ■ Proposition 1 has a direct engineering meaning: the boundary's isolation is set by the power path and the terminations, not by the switch. With matched terminations, isolation of I dB requires $|Z_0 + Z_P| \geq 1/2\, Z_0\, 10^{I/20}$, i.e. roughly 250 Ω for 20 dB and 2.5 kΩ for 40 dB. Because the power path must also carry the load current at 50 Hz, its design trades a negligible mains-frequency impedance against a high RF impedance, complicated by self-resonance. Fig. 3 plots both expressions, treating Z_P as resistive, with the measured parts of Section VII-C. For the selected inductor, evaluating (5) with the measured complex Z_P gives -23.8 dB at the frequency of minimum $|Z_P|$ and a median of -24.5 dB over the band, compared with the measured median of -23.27 dB.

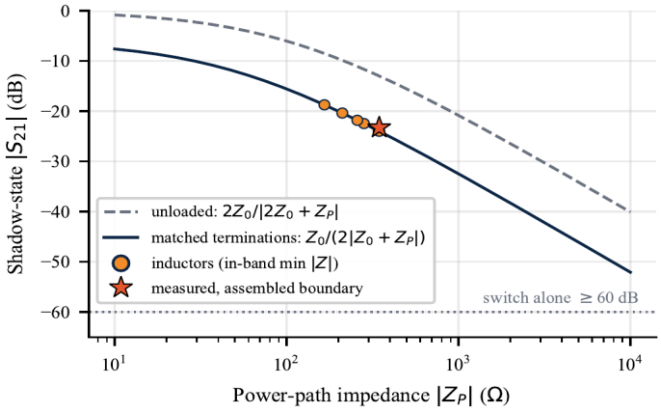


Fig. 3. Shadow-state transmission versus power-path impedance: unloaded expression (4) and matched-termination expression (5) for resistive Z_P, the measured inductors at their minimum in-band $|Z_P|$, and the assembled boundary (median shadow-state transmission plotted at the inductor's minimum in-band $|Z_P|$). The switch's own isolation (≥60 dB) is not the limiting factor.

 © Author(s) | CC BY 4.0 International License.

iJETRM
INTERNATIONAL JOURNAL OF ENGINEERING TECHNOLOGY RESEARCH & MANAGEMENT (IJETRM)
https://ijetrm.com/

C. Isolation Change

Because $|S_{21}|$ also depends on the lines and loads connected outside the boundary, we characterise the intervention by the ratio of shadow to through transmission measured at the same reference planes,

$$\kappa(f) = 20\log_{10}\frac{|S_{21}^{S}(f)|}{|S_{21}^{O}(f)|} \quad \text{dB}, \qquad (6)$$

which removes common factors such as cable loss.

D. Diagnostic Band Selection

A shadow state is useful only where both ports are terminated (so that the open switch does not create reflections that masquerade as anomalies) and the power path leaks little. We define the admissible band

$$\mathcal{B} = \{f:\ |S_{11}^{H,S}| \le \tau,\ |S_{11}^{L,S}| \le \tau,\ 2Z_0/|2Z_0 + Z_P| \le \tau\}, \qquad (7)$$

with $\tau = 10^{-10/20} \approx 0.32$ (i.e. -10 dB) in this work. A series blocking capacitance C_b in the RF path, required to exclude mains energy, sets a further lower limit of roughly $f \gtrsim 1/(2\pi C_b \cdot 2Z_0)$, about 21 MHz for $C_b = 75$ pF.

E. Time-Domain Analysis

Given a reflection difference $\Delta S_{11}(f_k) = S_{11}(f_k) - \bar{S}_{11}(f_k)$ relative to a baseline mean, we form the band-pass time-domain response

$$\Delta h(t) = \frac{\left|\sum_k w_k\ \Delta S_{11}(f_k)\ e^{j2\pi f_k t}\right|}{\sum_k w_k}, \qquad (8)$$

with a Hann window w_k. For a band of width B and spacing Δf, the nominal resolution is $1/B$ and the unambiguous range is $1/\Delta f$; the window broadens the main lobe to about $2/B$. A peak at round-trip time t_p corresponds to a distance $d = v_p\, t_p/2$ from the reference plane, where v_p is the propagation velocity.

V. Diagnostic Method

This section describes the method as proposed. The bench study of Section VI implemented a subset of it: the RF state was set by hand, the house view was acquired in the order through then shadow, the state variables $\boldsymbol{q}$, mains alignment, health and topology checks and de-embedding were not implemented, and the validity conditions were represented by the measurement gates of Section VI-E.

A. Sequence and Validity Conditions

Fig. 4 shows the intervention. After an anomaly is detected against predetermined criteria, the controller selects an observable boundary, records the pre-intervention state $\boldsymbol{q}_0$, and executes RF-through, RF-shadow, RF-through aligned to the mains phase and within the anomaly coherence time τ_c. The power path remains conductive throughout. The controller then evaluates the validity conditions:

1. *Isolation:* the measured effective isolation, in both directions and including alternative paths, satisfies a pre-set minimum;
2. *Invariance:* $\| \boldsymbol{q} - \boldsymbol{q}_0 \|$ remains within tolerance throughout, and the two RF-through observations agree;
3. *Health:* receivers and sensing paths pass self-checks;
4. *Topology and model fit:* the installation matches its recorded topology and the observation fits the response space characterised at installation;
5. *Uniqueness and safety:* no unresolved multiple anomaly and no unsafe condition is present.

Failure of any condition sets $\rho = 0$.

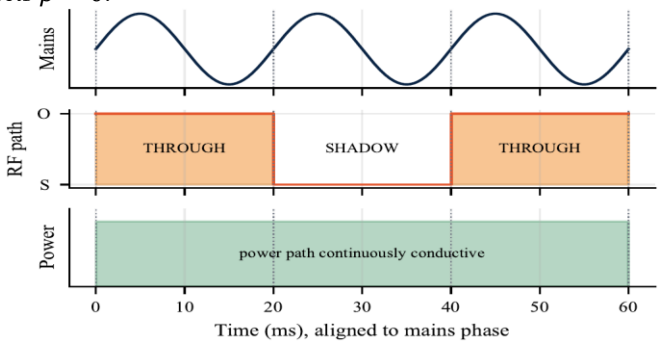


Fig. 4. Intervention timing: the RF path is switched THROUGH (O), SHADOW (S), THROUGH (O) in alignment with the mains cycle while the power path remains continuously conductive (conceptual; not implemented in the bench study).

 © Author(s) | CC BY 4.0 International License.

iJETRM
INTERNATIONAL JOURNAL OF ENGINEERING TECHNOLOGY RESEARCH & MANAGEMENT (IJETRM)
https://ijetrm.com/

B. Features and Thresholds

In the proposed method the known responses of couplers, the switch and interconnections are first de-embedded; in the bench study no couplers were used and no de-embedding was applied. The residual for view v and state s is the root-mean-square (RMS) complex deviation from the baseline mean over the K analysed frequency points:

$$r_{v,s} = \left(\frac{1}{K} \sum_{k=1}^{K} \left| S_{11}^{(v,s)}(f_k) - \bar{S}_{11}^{(v,s)}(f_k) \right|^2 \right)^{1/2} . \qquad (9)$$

With M baselines $b = 1, \ldots, M$, the threshold is set at twice the largest baseline deviation:

$$T_{v,s} = 2 \max_b r_{v,s}^{(b)} . \qquad (10)$$

Here $r_{v,s}^{(b)}$ is the residual of baseline b against the mean of all M baselines, including b itself. Because each baseline contributes to the mean, its deviation is smaller than that of an independent trial (by about $\sqrt{(M-1)/M}$, i.e. 0.82 for $M = 3$), so (10) tends to be low when M is small; a leave-one-out definition would avoid this. The persistence ratio $\psi = r_{H,S}/r_{H,O}$ measures whether a house-end residual survives RF isolation of the load side: a house-side source should give $\psi \approx 1$.

C. Decision Rules

Let $\mathbb{1}_{v,s} = [r_{v,s} \geq T_{v,s}]$. Two rules, used in Trial B, were specified before its data collection.

Rule A (strict, primary). Attribute to H_W if $\mathbb{1}_{H,O} \wedge \mathbb{1}_{H,S} \wedge (\psi \geq 0.5) \wedge \neg\mathbb{1}_{L,S}$; to H_L if $\mathbb{1}_{H,O} \wedge \neg\mathbb{1}_{H,S} \wedge \mathbb{1}_{L,S}$; to H_0 if $\neg\mathbb{1}_{H,O} \wedge \neg\mathbb{1}_{L,S}$; otherwise abstain. Rule A requires load-side evidence for any load-side output, and a load-side shadow residual below threshold for a wiring output.

Rule B (two-sided, secondary). As Rule A, except that H_L is output if $\mathbb{1}_{L,S} \wedge \neg\mathbb{1}_{H,S}$, i.e. without requiring a house-end through residual.

Trial A classifier. Trial A used an earlier, house-view-only classifier: no anomaly if $\neg\mathbb{1}_{H,O}$; otherwise fixed wiring if $\mathbb{1}_{H,S} \wedge (\psi \geq 0.5)$; otherwise load-side consistent if $\neg\mathbb{1}_{H,S}$; otherwise not attributable. Because a load-side output requires load-side evidence that a house-only view cannot provide, a load-side-consistent output is reported as *not attributable*.

In all rules, any failed validity condition yields *not attributable*. The decision logic is summarised in Algorithm 1 and Fig. 5.

Algorithm 1: Continuous-power boundary attribution
Input: anomaly trigger; installation baselines, thresholds and hypothesis regions.
1: Select boundary; record $\mathbf{q}_0$.
2: Acquire $S^{(v,O)}$; switch RF path to S; acquire $S^{(v,S)}$; switch to O; reacquire. Power path stays on.
3: Compute effective isolation κ (both directions); **if** insufficient **return** not attributable.
4: **if** $\mathbf{q}$ changed, through observations disagree, or health/topology/safety checks fail **return** not attributable.
5: De-embed; compute $r_{v,s}$ (9) and ψ.
6: Apply decision rule; **if** no unique hypothesis is supported **return** not attributable.
7: **return** attributed hypothesis with supporting evidence.

 © Author(s) | CC BY 4.0 International License.

iJETRM
INTERNATIONAL JOURNAL OF ENGINEERING TECHNOLOGY RESEARCH & MANAGEMENT (IJETRM)
https://ijetrm.com/

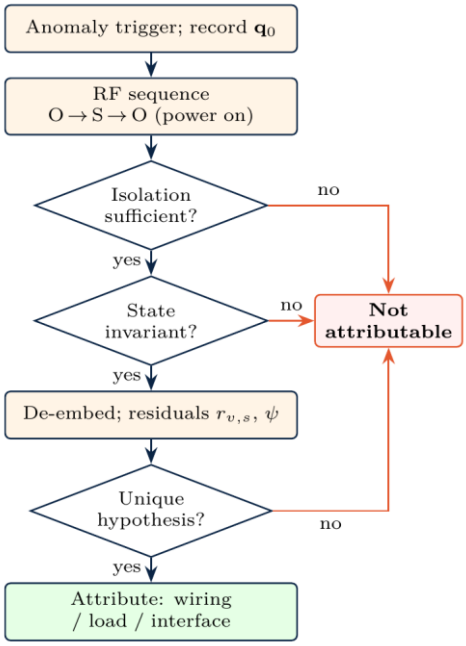


Fig. 5. Decision logic with mandatory abstention. Any failed validity condition or non-unique evidence yields not attributable.

VI. EXPERIMENTAL METHODOLOGY

A. Instrumentation and Calibration

Measurements used a NanoVNA-H4 vector network analyser (VNA; firmware 1.2.44) at 401 points with a 100 Hz intermediate-frequency bandwidth. Short-open-load-through (SOLT) calibration was performed in two ranges, 50 kHz–10 MHz (low frequency, LF) and 1–300 MHz (high frequency, HF), without isolation calibration and with the unmarked standards treated as ideal. The port-1 reference plane was the face of a barrel adaptor on the port-1 cable and the port-2 plane the end of the port-2 cable. Touchstone data were exported over USB. Calibration was verified by direct-through measurement, an attenuator cross-check, ten repeated sweeps, connector re-mating and drift tests (Table III). Analyser screenshots are reproduced only where they were checked against the corresponding data.

TABLE III: Calibration Verification

Check	LF range	HF range	Limit
Direct-through $\lvert S_{21}\rvert$ deviation	0.003 dB	0.057 dB	≤0.20 dB
Direct-through $\lvert S_{11}\rvert$ (worst)	−42.0 dB	−30.7 dB	≤ −30 dB
Attenuator cross-check[a]	−9.67 to −9.71 dB	−9.64 to −9.78 dB	−10 ± 1 dB
Trace noise $\lvert S_{21}\rvert$, worst-bin SD[b]	0.001 dB	0.029 dB	≤0.05 dB
Re-mating (calibration load, 5 refits), complex SD	1.53×10^{-4}	2.62×10^{-4}	recorded
Through drift, S_{21} (incl. one reconnection)	1.3×10^{-3} / 18 min	7.7×10^{-3} / 10 min	recorded

SD: standard deviation. [a]Measured with calibrations about 12 h old. [b]Direct through used in place of the attenuator.

B. Measurement Uncertainty

Following the Guide to the Expression of Uncertainty in Measurement (GUM) [15], we identify the components that contribute to the residual (9): instrument noise, connector re-mating, drift, and the variability introduced by physically remaking the substitution joints between trials (*handling*). Table IV compares them with the observed effects. Handling exceeds instrument noise and re-mating by more than two orders of magnitude and the through drift by about a factor of five, which is why the threshold rule (10) is derived from baselines acquired with the same handling as trials. Fig. 6 visualises the hierarchy.

 © Author(s) | CC BY 4.0 International License.

iJETRM
INTERNATIONAL JOURNAL OF ENGINEERING TECHNOLOGY RESEARCH & MANAGEMENT (IJETRM)
https://ijetrm.com/

TABLE IV: Residual Uncertainty Components (HF Range, House View)

Component	Magnitude (linear)
Trace noise (S_{11}, worst-bin SD, 10 sweeps)	2.57×10^{-4}
Connector re-mating (calibration load, SD)	2.62×10^{-4}
Through drift, S_{21}, 10 min (incl. reconnection)	7.7×10^{-3}
Handling, Trial B baselines (max deviation, through)	3.6×10^{-2}
Decision threshold $T_{H,0}$, Trial B	7.27×10^{-2}
Largest residual, no-fault and load-side trials (pooled)	0.135
Smallest residual, wiring-side trials (pooled)	0.510

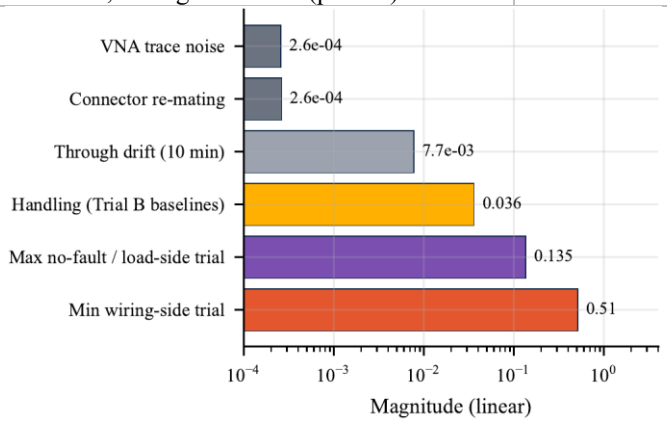


Fig. 6. Hierarchy of residual magnitudes, from instrument noise to the wiring-side effect (log scale). The drift entry refers to S_{21}; all others to S_{11}.

C. Boundary Hardware

The RF path used an HMC849-marked single-pole double-throw (SPDT) switch board powered from a 3.3 V supply, with its control input set by a jumper moved by hand. The common port (RFC) faced the house side; RF1 connected to the load side in RF-through; in RF-shadow the switch connected RFC to RF2, terminated in 50 Ω, while RF1 was terminated by the switch's internal absorptive load. The power-path inductor was connected across the RFC and RF1 centre conductors on the connector side of the board's blocking capacitors, so that it remained in circuit in both states.

D. Line Analogue and Fault Substitutes

Fig. 7 shows the arrangement. A two-core cable of approximately 25 m connected the house-end observation point to the boundary, with an unpowered W5W lamp as the load. One of two 4 Ω, 25 W aluminium-housed resistors could be inserted in series at a wiring-side point on the short house-end lead (condition W) or at a load-side point adjacent to the lamp (condition L); otherwise both points were joined directly (condition N). Resistors of this construction are likely to be appreciably inductive at 190–300 MHz, so the substitutes are not small series resistances at the diagnostic frequencies; their RF impedance was not measured. The house view connected the calibrated analyser port to the house end; the load view connected it to the boundary's load-side port (RF1). All work was unpowered, at milliwatt RF levels, and no connection to mains was made.

 © Author(s) | CC BY 4.0 International License.

iJETRM
INTERNATIONAL JOURNAL OF ENGINEERING TECHNOLOGY RESEARCH & MANAGEMENT (IJETRM)
https://ijetrm.com/

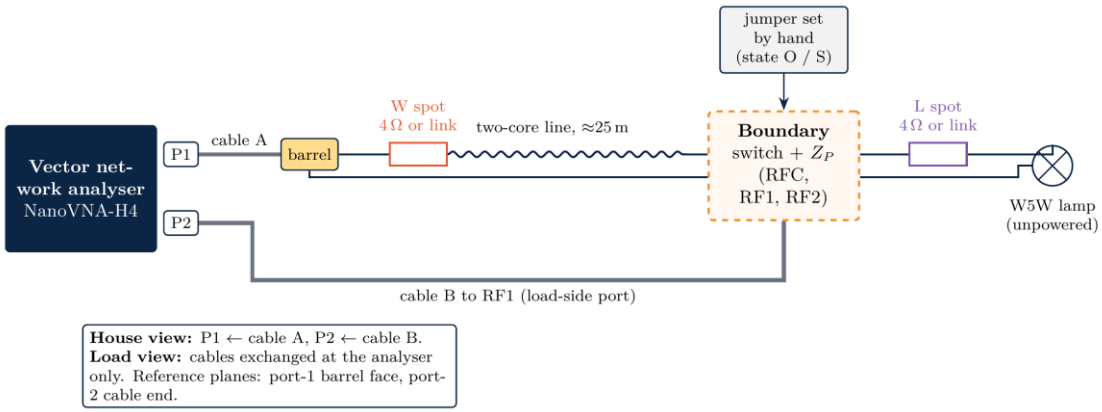


Fig. 7. Measurement set-up of the line analogue (schematic). The analyser observes the house end through cable A and the boundary's load-side port through cable B; views are exchanged at the analyser without touching the fixture. Series 4 Ω substitutes are inserted at the wiring-side (W) or load-side (L) spot.

E. Trial Design and Research Integrity

Table V summarises the two trials and Fig. 8 the protocol. For each trial series the author prepared a balanced, randomised condition list, kept it private, and set each condition by hand. The analysis protocol, features, threshold rule and decision rules were fixed and recorded with a time stamp before the trial data were acquired [19], and classification ran as a frozen script on the exported data. All classifications were recorded before the list was revealed [20]. Blinding applied to the analysis.

Each capture was checked by a 50 kHz loop-resistance measurement and a switch-state check; Trial B added an in-situ isolation check ($\kappa \leq -10$ dB), a view check and a screenshot at every capture. Captures failing a check were repeated.

A preliminary run was excluded after inspection showed a fixture fault at the reference plane.

In Trial B, following a change in the fixture, the baselines used for the thresholds (B4–B6) were acquired after the last trial, and a drift check introduced during the trial was not used for exclusion because its outcome was correlated with the wiring-side condition. All protocol changes were made before classification and before the condition list was revealed.

TABLE V: Trial Design

	Trial A	Trial B
Views	House	House and load
Captures per trial	2	4
Baselines	3, before trials	3, after last trial
Valid trials (N/W/L)	12 (4/4/4)	11 (4/4/3)[a]
Gates	loop R, switch	loop R, switch, isolation, view
Screenshots	–	every capture
Classifications recorded before unblinding	Yes	Yes

[a]One L trial excluded after a fixture change.

 © Author(s) | CC BY 4.0 International License.

iJETRM
INTERNATIONAL JOURNAL OF ENGINEERING TECHNOLOGY RESEARCH & MANAGEMENT (IJETRM)
https://ijetrm.com/

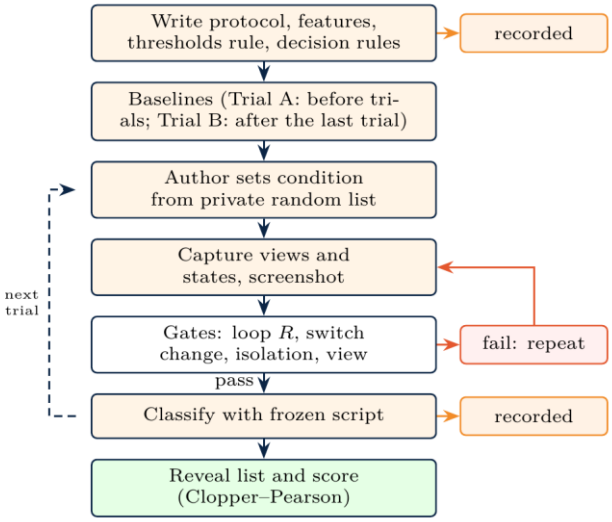


Fig. 8. Protocol of the blinded trials. The threshold and decision rules are fixed before data, and classifications are recorded before the condition list is revealed.

F. Data Processing

All analysis operates on the exported Touchstone files; raw data were never edited. Each trial's captures were parsed and the complex reflection coefficients compared with the baseline mean of the same view and state using (9) over an analysis band of 190–300 MHz (148 points from 190.1 MHz). This band was adopted before the inductor survey and is slightly wider than $\mathcal{B}$ (193.1–300 MHz, 144 points; Section VII-D). The in-situ isolation change of each trial was evaluated as the median of κ over the analysis band. Thresholds were computed from the baselines only, before any trial was classified, and the classification script was frozen together with the analysis plan. Time-domain responses were computed with (8) over the full 1–300 MHz sweep on a 0.5 ns grid. The scripts that generate every figure and statistic in this paper read the raw files directly.

G. Statistical Analysis

Proportions are reported with exact Clopper–Pearson 95% intervals [16]. Separation between conditions on the house-end residual is quantified by the area under the receiver operating characteristic (AUC) and an exact one-sided Mann–Whitney test [17]; for complete separation of n_1 and n_2 observations the exact p-value is $1/\binom{n_1+n_2}{n_1}$. Effect size is reported as Cohen's d [18] on $\log_{10} r$. Pooled and time-domain analyses were defined after unblinding and are identified as post hoc. The pooled observations come from two fixtures and two baseline sets, and the residuals within each trial series share a baseline mean, so they are not fully independent. The p-value is therefore descriptive rather than confirmatory.

VII. RESULTS

A. Calibration

All applicable verification limits were met (Table III). The HF direct-through match was marginal above about 200 MHz (-30.7 dB worst case), which is acceptable for differential residual features but limits absolute accuracy. The calibration standards were uncharacterised, so absolute traceability is not claimed.

B. RF Switching Network

Fig. 9 shows the switch alone. Through-path insertion loss was 0.58–0.72 dB over 75–300 MHz; isolation between selected and unselected paths exceeded 60 dB above 30 MHz, limited by the instrument floor; forward and reverse transmission agreed within 0.03 dB. The unselected port presented approximately 48 Ω in series with about 25 pF, with $|S_{11}| = -3.6, -8$ and -14 dB at 76, 150 and 300 MHz. With 50 Ω on RF2, the house port in shadow reached $-13, -20$ and -27 dB at the same frequencies. The equivalent series blocking capacitance was about 75 pF, making RF transfer usable above about 20–30 MHz.

 © Author(s) | CC BY 4.0 International License.

iJETRM
INTERNATIONAL JOURNAL OF ENGINEERING TECHNOLOGY RESEARCH & MANAGEMENT (IJETRM)
https://ijetrm.com/

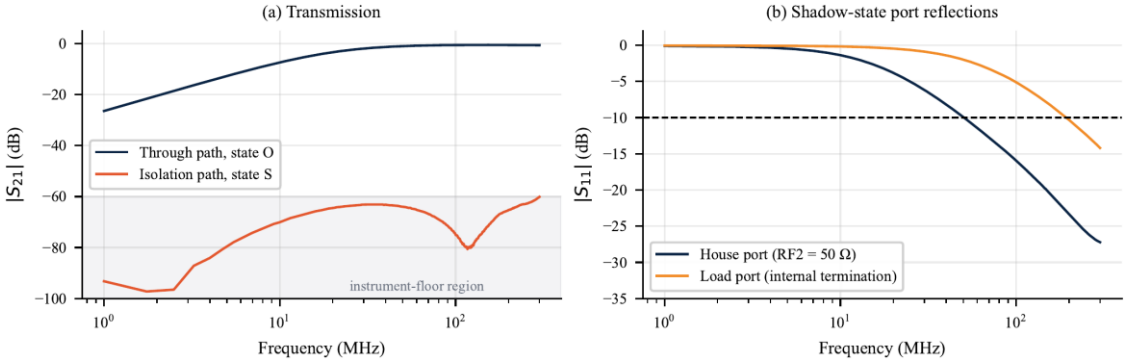


Fig. 9. RF switching network characterised in isolation: (a) through-path and isolation-path transmission; (b) shadow-state reflections of the house port (RF2 terminated in 50 Ω) and the load port (internal termination).

C. Power-Path Inductors and Isolation Budget

Seven candidate inductors were measured in a shunt fixture (Table VI, Fig. 10). Two parts labelled 100 µH measured about 21 µH, illustrating the need for incoming verification. Applying the unloaded expression (4) to the minimum in-band impedance magnitude, i.e. treating Z_P as resistive, gives leakage values between -8.5 and -13.0 dB. This is the most favourable case; with the measured complex Z_P the leakage is slightly higher (e.g. -12.6 dB for the 47 µH part). The 47 µH part offered the highest minimum impedance and was selected by the pre-set rule.

TABLE VI: Power-Path Inductor Survey and Leakage Bound

Label	L (µH)	SRF (MHz)	$\lvert Z\rvert_{\max}$ (Ω)	$\min_{\mathcal{B}}\lvert Z\rvert$ (Ω)	Leakage[a] (dB)
10 µH	10.0	96.7	792	343	−12.9
22 µH	19.0	50.3	1275	282	−11.6
33 µH	33.0	32.4	1671	211	−9.9
47 µH	**41.6**	**19.7**	**1514**	**346**	**−13.0**
100 µH (A/B)	≈21	≈47–50	1170–1230	258–263	−11.1/−11.2
220 µH	180.7	4.7	2845	166	−8.5

SRF: self-resonant frequency. [a]Unloaded expression (4) at $\min_{\mathcal{B}}\lvert Z\rvert$, treating Z_P as resistive.

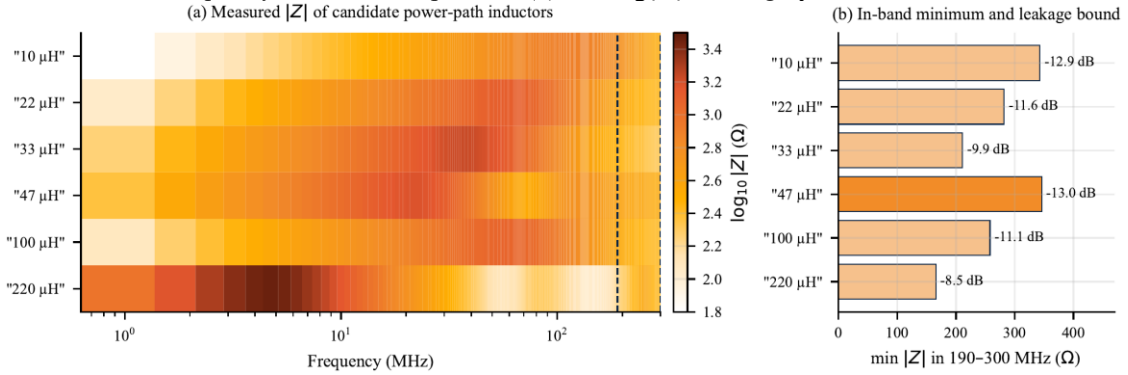


Fig. 10. Power-path inductor survey: (a) measured impedance of each candidate across 1–300 MHz (heat map; dashed lines bound the diagnostic band); (b) minimum in-band impedance and the corresponding unloaded leakage (resistive approximation). The 47 µH part (highlighted) was selected.

D. Diagnostic Band

The criterion (7) was first evaluated with an early candidate inductor and re-evaluated with the selected 47 µH part (Fig. 11); both give 144 of 401 frequency points satisfying all three conditions, forming a contiguous band from 193.1 to 300 MHz. For the selected part, tightening the leakage condition to -15 dB leaves no admissible point, so the power path is the binding constraint (a 10 µH part would retain 45 points). The slightly wider analysis band of 190–300 MHz, adopted earlier, was used in all subsequent experiments.

 © Author(s) | CC BY 4.0 International License.

iJETRM
INTERNATIONAL JOURNAL OF ENGINEERING TECHNOLOGY RESEARCH & MANAGEMENT (IJETRM)
https://ijetrm.com/

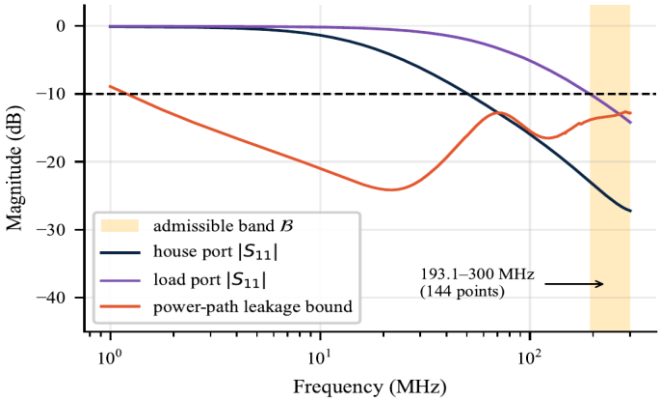


Fig. 11. Band-selection criterion (7): shadow-state port reflections and power-path leakage bound; shaded where all three are below −10 dB (193.1–300 MHz, 144 points).

E. Assembled Boundary

With the 47 µH inductor permanently connected, three RF-through/RF-shadow cycles were measured, each state as the per-point median of two sweeps, and sham handling without switching was performed in both states. Table VII gives the results, and Figs. 12 and 13 show the responses. Over 190–300 MHz the through and shadow transmissions were -0.73 and -23.27 dB, giving $\kappa = -22.5$ dB in each cycle, with a cycle-to-cycle spread not exceeding 0.021 dB and a sham effect not exceeding 0.006 dB, so the observed change is attributable to switching rather than handling. The shadow response predicted by (2)–(3) from the separately measured switch terminations and inductor agreed with the measurement within 0.55 dB at every one of the 148 analysed points, with a systematic offset of $+0.43$ dB (median, measured minus predicted; Fig. 12, lower panel). For the bench embodiment this answers RQ1: the change is large, repeatable and predictable, and the shadow-state transmission (-23.27 dB) is set by the power path, not by the switch ($\geq$60 dB isolation), as Proposition 1 predicts.

TABLE VII: Assembled Boundary, 190–300 MHz

Quantity	Measured
$\lvert S_{21}\rvert$, RF-through (median)	-0.73 dB
$\lvert S_{21}\rvert$, RF-shadow (median)	-23.27 dB
κ, each of three cycles	-22.5 dB
Cycle-to-cycle spread of κ	≤ 0.021 dB
Sham handling effect	≤ 0.006 dB
House-port $\lvert S_{11}\rvert$, through / shadow	≤ -17.7 / ≤ -18.6 dB
κ at 30 / 76 / 150 MHz	-25.3 / -18.5 / -24.3 dB
Measured minus model, shadow	max 0.55 dB; median $+0.43$ dB

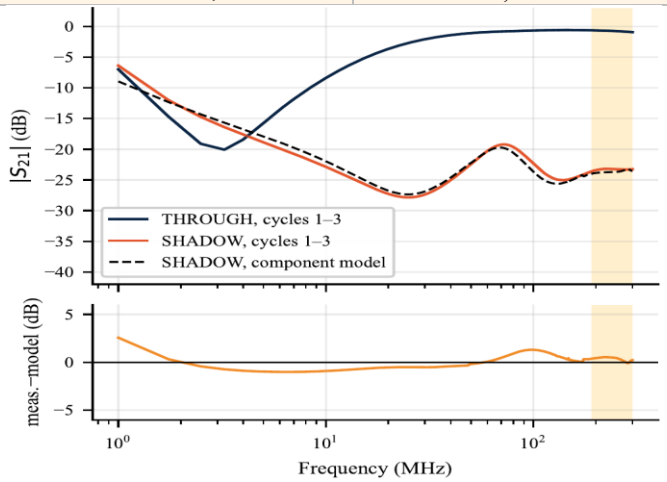


Fig. 12. Assembled boundary with the 47 µH power path permanently connected. Upper: $|S_{21}|$ in THROUGH and SHADOW for three cycles and the SHADOW response predicted from separately measured components. Lower: measured minus predicted SHADOW response.

 © Author(s) | CC BY 4.0 International License.

iJETRM
INTERNATIONAL JOURNAL OF ENGINEERING TECHNOLOGY RESEARCH & MANAGEMENT (IJETRM)
https://ijetrm.com/

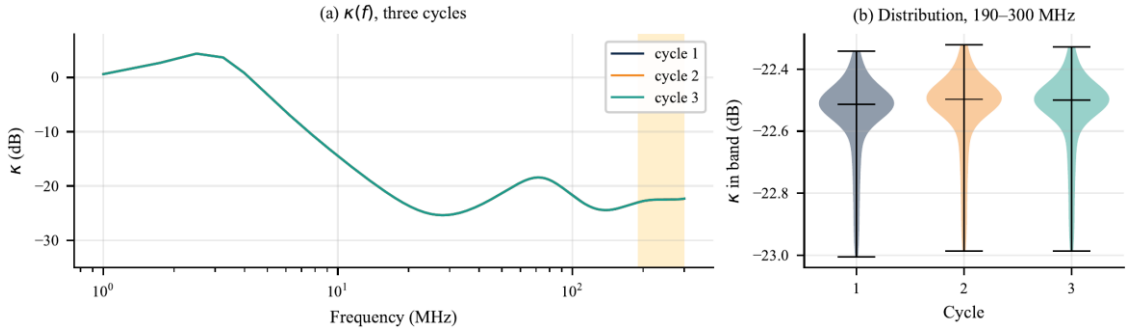


Fig. 13. Isolation change κ (6): (a) frequency response for three cycles (indistinguishable at this scale); (b) distribution of κ across the 190–300 MHz band for each cycle (violin plots with medians).

F. Line Analogue

In a preliminary set-up, the house-to-load transmission changed by about 20 dB between states over 30–300 MHz. A path-loss calculation from those measurements estimated that a load-side 4 Ω substitute would appear at the house end at about −86 dB, below the measurement floor. This predicted, before the trials, that load-side evidence must be acquired at a load-side observation point. Fig. 14 shows the no-fault baselines of Trial B, and Fig. 15 analyser captures of one of them; the screenshot values were checked against the corresponding data.

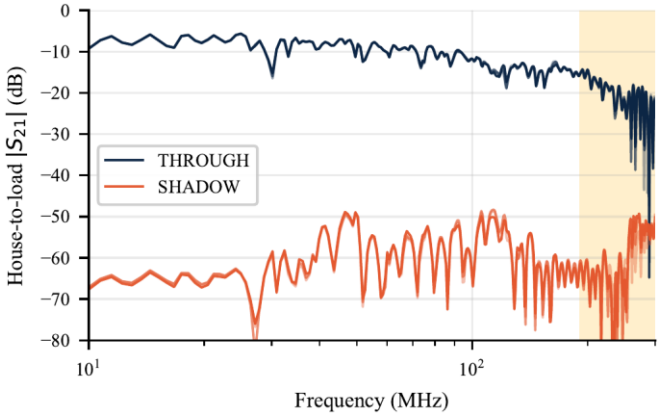


Fig. 14. House-to-load $|S_{21}|$ through the 25 m line analogue with the boundary in RF-through and RF-shadow (three no-fault baselines, Trial B).

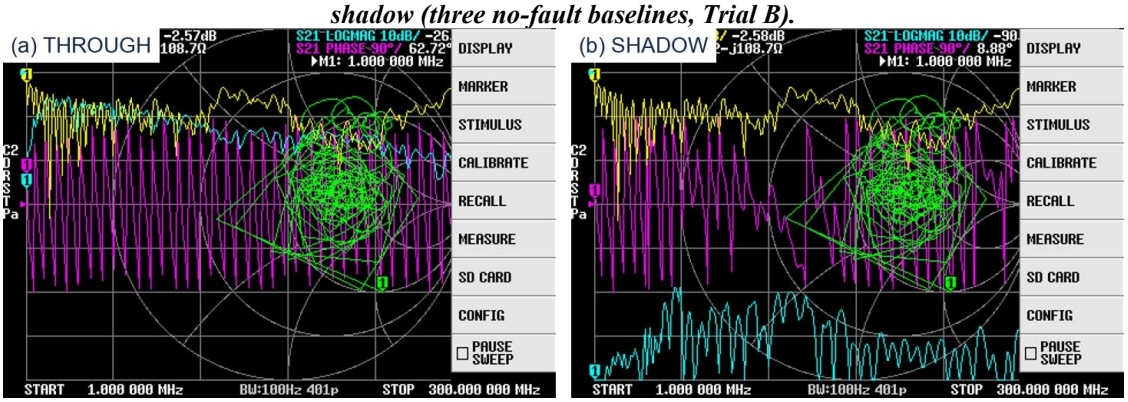


Fig. 15. Analyser captures of Trial B baseline B4 through the line: (a) RF-through, (b) RF-shadow.

G. Trial A: House-End View

Table VIII gives the outcomes of the Trial A classifier (Section V-C). The wiring-side substitute was attributed to fixed wiring in 4/4 trials (95% confidence interval (CI) 0.40–1.00), with $r_{H,O} = 0.611$–0.670 and $\psi = 1.007$–1.010. The threshold $T_{H,O} = 9.53 \times 10^{-3}$, derived from baselines that did not include the full handling of a trial, was smaller than the trial-to-trial variation: non-wiring residuals reached 0.135, and 6/8 non-wiring trials were also flagged as fixed wiring (95% CI 0.35–0.97). Deriving thresholds from handling-representative baselines, as in Trial B, addresses this. The load-side anomaly was indistinguishable from no fault at the house end, as predicted in Section VII-F.

 © Author(s) | CC BY 4.0 International License.

iJETRM
INTERNATIONAL JOURNAL OF ENGINEERING TECHNOLOGY RESEARCH & MANAGEMENT (IJETRM)
https://ijetrm.com/

TABLE VIII: Trial A Outcomes

True condition	Fixed wiring	Not attributable[a]	No anomaly	$\tau_{H,O}$ range
W (4)	**4**	0	0	0.611–0.670
L (4)	3	1	0	0.011–0.122
N (4)	3	0	1	0.008–0.135

[a]Load-side consistent; reported as not attributable because no load-side view was available.

H. Trial B: Two-Sided View

The thresholds from B4–B6 were $T_{H,O} = 7.27 \times 10^{-2}$, $T_{H,S} = 7.56 \times 10^{-2}$, $T_{L,O} = 4.80 \times 10^{-2}$ and $T_{L,S} = 9.08 \times 10^{-4}$. The house-view thresholds reflect handling, but the load-view shadow threshold was degenerate: the three baselines were nearly identical in that state, and every trial exceeded it. The wiring-side residual was 0.510–0.554 against 0.019–0.081 for all other trials, with $\psi = 0.994$–1.001.

Table IX and Fig. 16 give the outcomes. Because every trial exceeded $T_{L,S}$, neither the fixed-wiring nor the no-anomaly output was reachable. Rule A therefore abstained in all eleven trials, including the four wiring-side trials, and made no false attribution. Rule B attributed all three L trials to the load side (95% CI 0.29–1.00) but also three of four N trials.

The 50 kHz loop resistance was 10.5–12.6 Ω (N), 13.0–14.1 Ω (L) and 16.2–16.6 Ω (W) (Fig. 17). The in-situ isolation change κ was -25.8 to -41.3 dB in every analysed trial (Fig. 18).

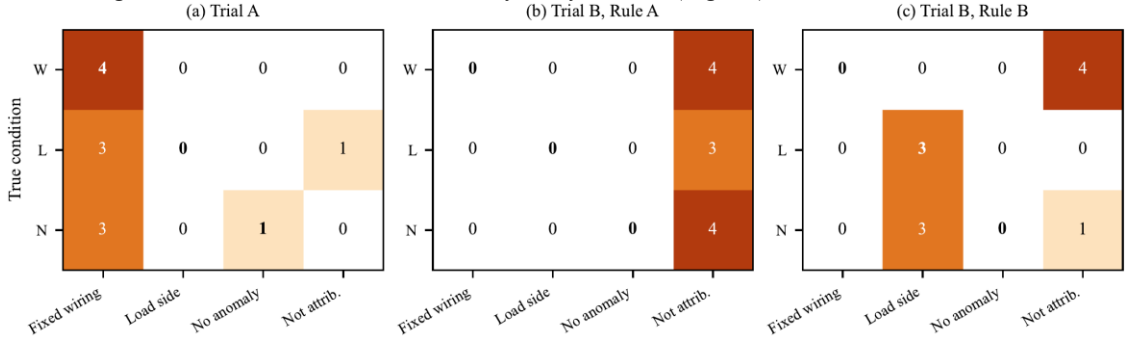


Fig. 16. Outcome matrices of the blinded trials (rows: true condition; columns: output; bold: correct class): (a) Trial A classifier (load-side-consistent outputs reported as not attributable); (b) Trial B, Rule A (strict); (c) Trial B, Rule B (two-sided).

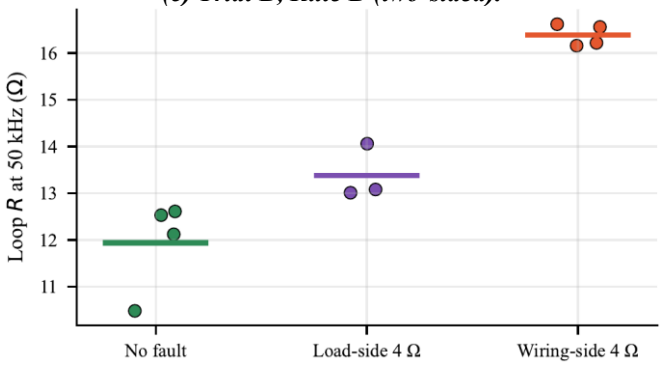


Fig. 17. Low-frequency loop resistance per Trial B trial (validity gate); horizontal lines: condition means.

TABLE IX: Trial B Outcomes

True condition	Rule A (strict)	Rule B (two-sided)
W (4)	Not attributable ×4	Not attributable ×4
L (3)	Not attributable ×3	Load side ×3
N (4)	Not attributable ×4	Load side ×3, not attributable ×1
False fixed-wiring attributions[a]	0/7	0/7
False load-side attributions	0/8	3/8

[a]With the load-view shadow threshold $T_{L,S}$, the fixed-wiring output was not reachable in this trial.

 © Author(s) | CC BY 4.0 International License.

iJETRM
INTERNATIONAL JOURNAL OF ENGINEERING TECHNOLOGY RESEARCH & MANAGEMENT (IJETRM)
https://ijetrm.com/

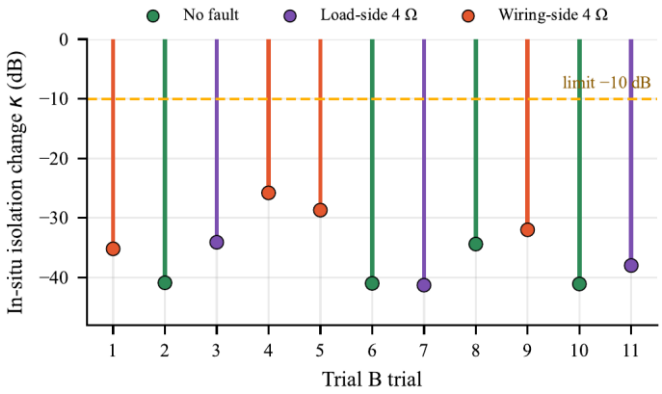


Fig. 18. In-situ isolation change κ (median over 190–300 MHz) in each analysed Trial B trial; dashed: gate limit.

I. Pooled House-End Separation (Post Hoc)

Pooling both trials (post hoc) gives eight W observations ($r_{H,O} = 0.510$–0.670) and fifteen non-W observations (0.0078–0.135), shown in Fig. 19 and Table X. The two groups are completely separated: AUC = 1.0, the smallest W residual exceeds the largest non-W residual by a factor of 3.78, and the exact one-sided Mann–Whitney $p = 1/\binom{23}{8} \approx 2.0 \times 10^{-6}$. On a logarithmic scale the mean residuals differ by 1.11 decades with a pooled standard deviation of 0.32, i.e. $d = 3.5$; for the reasons given in Section VI-G these statistics are descriptive. The persistence ratio lies within 1% of unity for all eight W trials. This is the behaviour expected of a house-side source; the wiring-side substitute also produced near-total reflection at the house end (house-end $|S_{11}|$ of -1.0 to -1.3 dB in the Trial B W trials, against -4.8 to -6.2 dB otherwise). A house-view rule requiring both $\mathbb{1}_{H,O}$ and $\mathbb{1}_{H,S}$ would have identified 4/4 W trials in Trial B with one marginal non-W exceedance ($r_{H,O} = 0.081$ against $T = 0.073$); this rule was not prospectively specified.

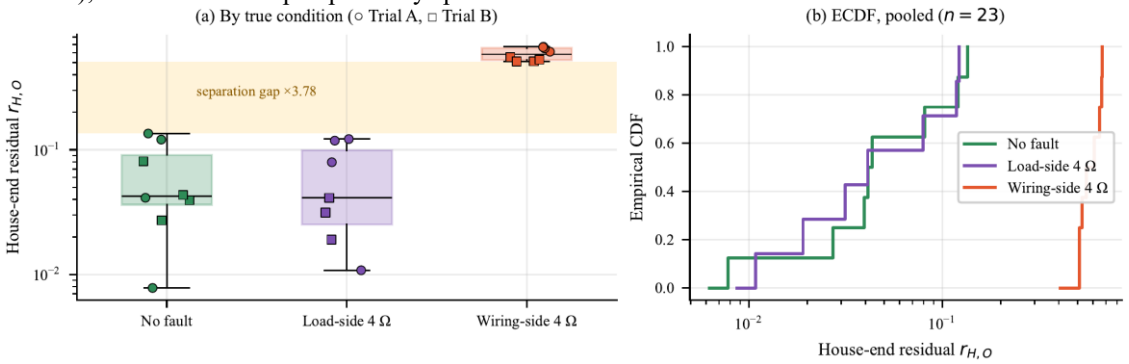


Fig. 19. House-end residual $r_{H,O}$ across both blinded trials: (a) box plots with individual trials (circles Trial A, squares Trial B) and the separation gap; (b) empirical cumulative distribution functions by condition.

TABLE X: Pooled House-End Separation (Post Hoc, Descriptive)

Statistic	Value
W trials / non-W trials	8 / 15
$r_{H,O}$, W (min–max)	0.510–0.670
$r_{H,O}$, non-W (min–max)	0.0078–0.135
Separation margin $\min r_W / \max r_{\bar{W}}$	3.78
AUC	1.00
Exact one-sided Mann–Whitney p	2.0×10^{-6}
Cohen's d on $\log_{10} r$	3.5
Persistence ratio ψ, W	0.994–1.010

J. Time-Domain Analysis (Post Hoc)

Applying (8) to the house-view through-state difference against the baseline mean ($B = 299$ MHz, $\Delta f = 0.7475$ MHz; nominal resolution 3.3 ns, Hann main lobe about 6.7 ns, unambiguous range 1.34 µs) gives the responses in Fig. 20. In all eight W trials the peak occurs at a round-trip time of 5.0 ns (Trial B) or 5.5 ns (Trial A), the difference being within the 0.5 ns evaluation grid and consistent with small fixture differences between trials,

 © Author(s) | CC BY 4.0 International License.

iJETRM
INTERNATIONAL JOURNAL OF ENGINEERING TECHNOLOGY RESEARCH & MANAGEMENT (IJETRM)
https://ijetrm.com/

with amplitudes of 0.82–0.95. All N and L trials have peaks of at most 0.10 (in Trial A clustered at 1–2 ns), and the Trial B baselines at most 0.015. For velocity factors between 0.66 and 1.0, the W peak corresponds to 0.50–0.82 m from the house-end reference plane, about fifty times earlier than the approximately 253 ns round trip to the far end of the line. The response therefore places the wiring-side residual near the house end of the line, within one main-lobe width of the reference plane.

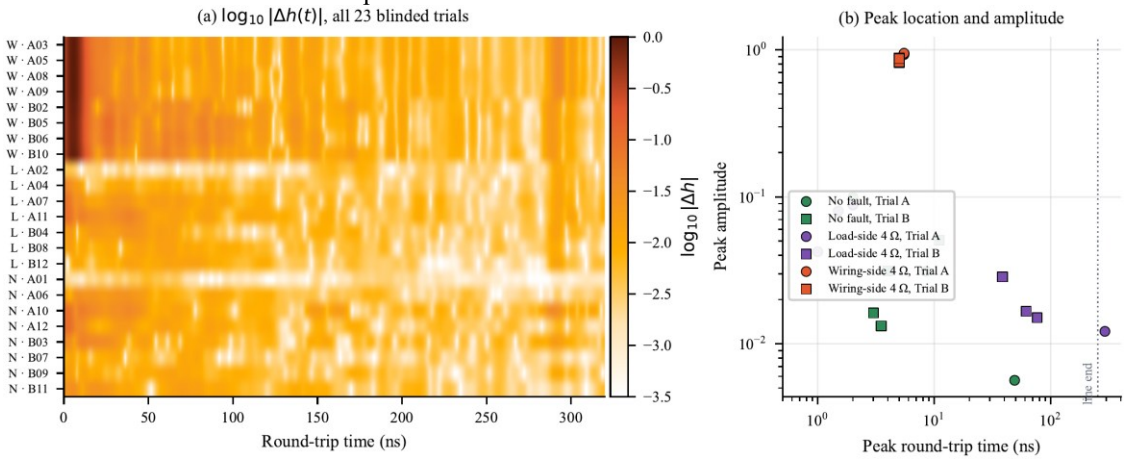


Fig. 20. Time-domain response of the house-end residual (post hoc): (a) $\log_{10}|\Delta h(t)|$ for all 23 blinded trials, grouped by true condition; (b) peak round-trip time and amplitude per trial. Every wiring-side anomaly peaks at 5.0–5.5 ns with amplitude 0.82–0.95; all other trials stay below 0.10.

K. Load-View Analysis

Fig. 21 shows the load-view residuals. The shadow-state residuals of the three conditions overlap ($r_{L,S}$: L 0.0043–0.0170, N 0.0077–0.0220, W 0.0084–0.0142), as do the through-state residuals (L 0.045–0.126, N 0.023–0.418, W 0.092–0.120). With the present arrangement, the load-side 4 Ω substitute is therefore not resolved from the load-side view. The loop resistance increase for L (about 1.4 Ω above N, against 4.4 Ω for W) suggests that the effective load-side substitution was smaller than nominal; the substitutes were not independently verified.

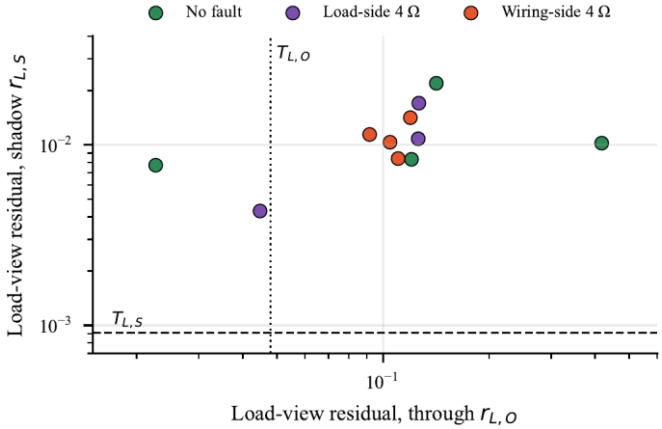


Fig. 21. Load-view residuals in through and shadow by true condition (Trial B); dashed and dotted lines: thresholds $T_{L,S}$ and $T_{L,O}$. The conditions are not separated.

L. Isolation-Gate Events

In two Trial B captures the in-situ isolation change fell to about −4 dB because a contact at the inductor bypassed the boundary. The isolation check identified these captures, which were repeated after correction (κ of −25.8 and −28.7 dB). Without an in-place isolation measurement (requirement R3), such captures would enter the classification.

VIII. DISCUSSION

A. Answers to the Research Questions

RQ1. On the unpowered bench, the boundary produced a 22.5 dB isolation change with its power path permanently connected, repeatable to 0.021 dB, unaffected by sham handling, and predictable from component measurements. Proposition 1 and the band criterion explain both its magnitude and its frequency range. *RQ2.* The house-side substitute was completely separated from the other conditions in 23 blinded trials on the house-end residual,

 © Author(s) | CC BY 4.0 International License.

iJETRM
INTERNATIONAL JOURNAL OF ENGINEERING TECHNOLOGY RESEARCH & MANAGEMENT (IJETRM)
https://ijetrm.com/

persisted in the shadow state, and appeared in the time domain near the house end (post hoc analysis, to be confirmed in a prospectively specified trial). *RQ3.* Load-side attribution requires a redesigned load-side view; with the present view the strict rule abstained in every case, because of a degenerate threshold, while the less strict rule attributed some no-fault trials to the load side.

B. Interpretation of the House-Side Signature

The persistence ratio of unity is consistent with a house-side origin, and the time-domain peak at 5.0–5.5 ns places the residual within about a metre of the house-end reference plane, on the lead where the substitute was inserted. Extending the trials to wiring-side anomalies further from the observation point is part of the next stage. The magnitude of the residual (0.5–0.7, corresponding to near-total reflection) is far larger than a purely resistive 4 Ω series element would produce, which indicates that the inductance of the 25 W resistor and the joint geometry dominate at 190–300 MHz. This does not affect the attribution logic, which depends on separation and persistence rather than on the absolute magnitude, but it implies that real degraded joints may present different magnitudes and must be characterised directly.

C. Requirements for Load-Side Attribution

Four factors, each testable, are consistent with the observations. (i) Termination masking: in shadow the load-side port is loaded by the switch's internal termination, which may dominate the load-side response and conceal a small series change beyond it. (ii) Lead inductance: at 190–300 MHz the reactance of the load-side leads exceeds a 4 Ω change by a large factor, compressing its relative effect. (iii) Connector repeatability: changing views required reconnecting the analyser, adding variability comparable to the expected effect. (iv) Baseline diversity: three nearly identical baselines produced a degenerate shadow threshold (9.1×10^{-4}), below the trial-to-trial variability. A smaller effective load-side substitution than nominal, suggested by the loop-resistance data, may also have contributed.

D. Design Implications

Proposition 1 shows how to raise isolation: increase $|Z_P|$ in the band (for example with distributed inductance or a resonant trap that preserves 50 Hz conduction), reduce switch off-capacitance, or cascade switching sections. The load-side observation point should present a defined termination that does not absorb the response of a load-side anomaly, use fixed connections, and be characterised with diverse baselines, with thresholds computed by leave-one-out. The isolation gate rejected bypassed captures and should be retained. The reject option should also be retained, but its thresholds must be derived from baselines that capture realistic variability, since in Trial B the strict rule abstained because of a degenerate threshold rather than because a validity check detected insufficient evidence.

E. Relation to Single-Point Reflectometry

The time-domain result invites the question whether a conventional single-point reflectometer would suffice. It localises a discontinuity along the propagation path from the access point, but it cannot by itself establish on which side of a connection point an anomaly lies when echoes from the wiring and the equipment overlap, and it cannot verify that the two sides were separated during the measurement. The boundary contributes three things that a single access point lacks: a controllable state change that isolates the load side, an in-place measurement of how well that isolation was achieved, and a persistence test that, for anomalies away from the observation point, can distinguish house-side from load-side origins. The two approaches are complementary, and the time-domain transform is naturally incorporated into the boundary method as a localisation feature.

F. Practical Deployment Considerations

Several factors govern translation to products. RF levels must respect electromagnetic compatibility limits and coexist with power-line communication, so the diagnostic sequence should be short, low-level and infrequent, triggered by anomaly detection rather than run continuously. Commissioning must capture baselines that represent the real variability of the installation, the lesson of Trial A. The coherence time of intermittent faults constrains the sequence duration, which motivates mains-phase alignment and completing the sequence within a few cycles; neither was implemented in this study. Finally, because responsibility for wiring and equipment differs, the system's output must carry its evidence (isolation achieved, invariance, residuals and localisation) so that an attribution can be audited.

G. Value of the Reject Option

Under the strict rule the system made no false attribution in eleven blinded trials, at zero coverage; Rule B attained coverage at the cost of three false load-side attributions. The contrast illustrates the coverage–risk trade-off of [13], [14]. Calibrating the abstention logic requires baselines that make every output of the rule reachable, which the redesigned load-side view will provide.

IX. LIMITATIONS

 © Author(s) | CC BY 4.0 International License.

iJETRM
INTERNATIONAL JOURNAL OF ENGINEERING TECHNOLOGY RESEARCH & MANAGEMENT (IJETRM)
https://ijetrm.com/

The measurements were unpowered and static, on a single line geometry, with blinding applied to the analysis. The resistive substitutes differ in their RF behaviour from real degraded joints, and the wiring-side substitute was close to the observation point. Samples are small; the pooled separation and time-domain analyses were defined after unblinding and will be confirmed in a prospectively specified replication. Operation under mains voltage and the interface hypothesis are the subject of the next stages.

X. FUTURE WORK

The programme continues in six stages: (i) a redesigned load-side observation point with defined termination, fixed connections and diverse baselines, evaluated in a prospectively specified blinded trial with the wiring-side substitute placed well away from the observation point, which also replicates the post hoc analyses; (ii) a boundary achieving $\kappa \leq -40$ dB through higher-impedance power paths and cascaded switching; (iii) an isolated low-voltage powered line to verify invariance of load current and voltage during switching; (iv) characterisation with real degraded and intermittent contacts in a safety enclosure; (v) an integrated socket-level prototype with automatic switching; and (vi) field evaluation under appropriate safety approval.

XI. CONCLUSION

This paper formulated electrical-anomaly source attribution as selective classification with a mandatory reject option and studied a continuous-power RF boundary intervention for it. A two-port analysis showed that the isolation of such a boundary is bounded by its power path, and a band criterion followed. An unpowered bench study agreed with the theory: a repeatable 22.5 dB isolation change with the power path permanently connected, within 0.55 dB of a component model. In two blinded trials, a wiring-side series substitute near the house end was completely separated from the other conditions on the house-end residual and appeared close to the house-end reference plane in the time domain (post hoc), and the in-situ isolation gate rejected bypassed captures. The load-side observations define the redesign needed for two-sided attribution. These results provide bench evidence for the physical basis of the method and set out its extension to two-sided attribution.

Appendix A: Derivation Details

Expanding (2) gives $A = 1 + Z_P Y_L$, $B = Z_P$, $C = Y_H + Y_L + Z_P Y_H Y_L$ and $D = 1 + Z_P Y_H$. Substituting in (3) yields the general shadow-state transmission used for the component model in Section VII-E, with Z_H, Z_L and Z_P taken from the measured one-port reflections Γ as $Z = Z_0(1 + \Gamma)/(1 - \Gamma)$. Setting $Y_H = Y_L = 0$ recovers (4).

Competing Interests

The author is employed by Avalon Artificial Intelligence Limited, the applicant for UK patent application GB 2625992.9 (unpublished), which covers the method described.

Data Availability

The data that support the findings of this study, comprising the raw S-parameter (Touchstone) measurements, analyser screenshots and the analysis scripts used to generate the figures and statistics, are available from the corresponding author upon reasonable request, subject to commercial confidentiality.

REFERENCES

[1] *General Requirements for Arc Fault Detection Devices*, BS EN 62606:2013, British Standards Institution, 2013.
[2] *Requirements for Electrical Installations. IET Wiring Regulations*, BS 7671:2018+A2:2022, Institution of Engineering and Technology and British Standards Institution, 2022.
[3] D. M. Pozar, *Microwave Engineering*, 4th ed. Hoboken, NJ, USA: Wiley, 2012.
[4] C. Furse, Y. C. Chung, C. Lo, and P. Pendayala, “A critical comparison of reflectometry methods for location of wiring faults,” *Smart Struct. Syst.*, vol. 2, no. 1, pp. 25–46, 2006.
[5] P. Smith, C. Furse, and J. Gunther, “Analysis of spread spectrum time domain reflectometry for wire fault location,” *IEEE Sensors J.*, vol. 5, no. 6, pp. 1469–1478, Dec. 2005.
[6] M. Zimmermann and K. Dostert, “A multipath model for the powerline channel,” *IEEE Trans. Commun.*, vol. 50, no. 4, pp. 553–559, Apr. 2002.
[7] M. Sapir, “Apparatus for the detection and early warning of electrical arcing fault,” U.S. Patent 6 667 691 B2, Dec. 23, 2003.
[8] J. Eriksen *et al.*, “Electrical receptacles, assemblies thereof, and end of life functionality,” U.S. Patent Appl. 2024/0332946 A1, Oct. 3, 2024.
[9] R. E. Teggatz *et al.*, “Electrical interconnect status monitoring system,” U.S. Patent 9 599 660 B2, Mar. 21, 2017.
[10] A. G. Sappok *et al.*, “Radio frequency process sensing, control, and diagnostics network and system,” U.S. Patent 10 799 826 B2, Oct. 13, 2020.

 © Author(s) | CC BY 4.0 International License.

iJETRM
INTERNATIONAL JOURNAL OF ENGINEERING TECHNOLOGY RESEARCH & MANAGEMENT (IJETRM)
https://ijetrm.com/

[11] L. Liao, Z. Liu, J. Du, and L. Hai, "A fault diagnosis method for pole-mounted circuit breakers based on multi-information fusion," CN Patent 121389025 B, Apr. 10, 2026 (assignee: Nanjing Ludian Intelligent Technology Co., Ltd.).
[12] B. Maxson and W. Miller, "Ingress noise localization in a cable network," U.S. Patent 8 724 681 B2, May 13, 2014.
[13] C. K. Chow, "On optimum recognition error and reject tradeoff," *IEEE Trans. Inf. Theory*, vol. IT-16, no. 1, pp. 41–46, Jan. 1970.
[14] Y. Geifman and R. El-Yaniv, "Selective classification for deep neural networks," in *Proc. Adv. Neural Inf. Process. Syst. 30 (NIPS)*, 2017, pp. 4878–4887.
[15] JCGM, *Evaluation of Measurement Data—Guide to the Expression of Uncertainty in Measurement*, JCGM 100:2008, 2008.
[16] C. J. Clopper and E. S. Pearson, "The use of confidence or fiducial limits illustrated in the case of the binomial," *Biometrika*, vol. 26, no. 4, pp. 404–413, 1934.
[17] H. B. Mann and D. R. Whitney, "On a test of whether one of two random variables is stochastically larger than the other," *Ann. Math. Statist.*, vol. 18, no. 1, pp. 50–60, 1947.
[18] J. Cohen, *Statistical Power Analysis for the Behavioral Sciences*, 2nd ed. Hillsdale, NJ, USA: Lawrence Erlbaum, 1988.
[19] B. A. Nosek, C. R. Ebersole, A. C. DeHaven, and D. T. Mellor, "The preregistration revolution," *Proc. Natl. Acad. Sci. USA*, vol. 115, no. 11, pp. 2600–2606, 2018.
[20] K. F. Schulz and D. A. Grimes, "Blinding in randomised trials: hiding who got what," *Lancet*, vol. 359, no. 9307, pp. 696–700, 2002.

 © Author(s) | CC BY 4.0 International License.